Soft Matter

PAPER

View Article Online
View Journal

Cite this: DOI: 10.1039/d1sm00184a

Shear stress dependence of force networks in 3D dense suspensions†

Lance E. Edens,[a] Enrique G. Alvarado,[a] Abhinendra Singh,[b] Jeffrey F. Morris,[c] Gregory K. Schenter,[d] Jaehun Chun[e] and Aurora E. Clark*[f]

The geometric organization and force networks of 3D dense suspensions that exhibit both shear thinning and thickening have been examined as a function of varying strength of interparticle attractive interactions using lubrication flow discrete element simulations. Significant rearrangement of the geometric topology does not occur at either the local or global scale as these systems transition across the shear thinning and shear thickening regimes. In contrast, massive rearrangements in the balance of attractive, lubrication, and contact forces are observed with interesting behavior of network growth and competition. In agreement with prior work, in shear thinning regions the attractive force is dominant, however as the shear thickening region is approached there is growth of lubrication forces. Lubrication forces oppose the attraction forces, but as viscosity continues to increase under increasing shear stress, the lubrication forces are dominated by contact forces that also resist attraction. Contact forces are the dominant interactions during shear thickening and are an order of magnitude higher than their values in the shear-thinning regime. At high attractive interaction strength, contact networks can form even under shear thinning conditions, however high shear stress is still required before contact networks become the driving mechanism of shear thickening. Analysis of the contact force network during shear thickening generally indicates a uniformly spreading network that rapidly forms across empty domains; however the growth patterns exhibit structure that is significantly dependent upon the strength of interparticle interactions, indicating subtle variations in the mechanism of shear thickening.

Received 3rd February 2021,
Accepted 8th July 2021

DOI: 10.1039/d1sm00184a

rsc.li/soft-matter-journal

1 Introduction

Dense suspensions that contain a high volume fraction of particles immersed in a liquid can exhibit a wide array of non-Newtonian rheology. This non-equilibrium behavior is influenced by a range of particle interactions, including the physicochemical characteristics of both the particles and the suspending medium. Suspended particles may generally be subject to hydrodynamic, van der Waals, electrostatic, Brownian, and frictional forces, each of which may predominate depending on the conditions.[1,2] Under an applied shear, different rheological behaviors, such as shear thinning and shear thickening, may be observed depending on the interplay of these forces and the system characteristics. Yielding and shear thinning under low applied stress can transition into shear thickening and shear-induced jamming at larger applied stress.[3]

Shear thinning is a nonlinear effect where increasing the applied shear stress to a suspension decreases the viscosity. This phenomenon is observed in applications of cement paste, ceramic precursors, or food products, and is not necessarily deleterious. Theories for the mechanism behind shear thinning focus on different physical aspects such as the breakdown of particle clustering, elastohydrodynamic interactions where particles overcome the lubrication forces opposing frictional contact, or upon possible non-Newtonian properties of the solvent.[3,4] Conversely, suspensions exhibiting shear thickening can flow relatively easily at low stress but become highly viscous as the applied shear stress increases. The impacts of shear thickening are often undesirable when handling dense suspensions in similar industrial settings. The shear thickening response can be continuous shear thickening (CST), where the viscosity increase with shear stress is gradual, or it can be discontinuous shear thickening (DST), where the

[a] Department of Chemistry, Washington State University, USA
[b] Levich Institute, CUNY City College of New York and Pritzker School of Molecular Engineering and James Franck Institute, The University of Chicago, USA
[c] Levich Institute and Department of Chemical Engineering, CUNY City College of New York, USA
[d] Pacific Northwest National Laboratory and Department of Chemistry, Washington State University, USA
[e] Pacific Northwest National Laboratory and Levich Institute/Department of Chemical Engineering, CUNY City College of New York, USA
[f] Department of Chemistry, Voiland School of Chemical Engineering and Bioengineering, Washington State University, and Pacific Northwest National Laboratory, USA. E-mail: auclark@wsu.edu

† Electronic supplementary information (ESI) available: Pictorial representations of analysis methods, expanded radial distribution functions and force network distributions under different attractive forces. See DOI: 10.1039/d1sm00184a

viscosity rises abruptly (often by orders of magnitude) at a critical shear rate. In the shear-jammed state, the suspension does not flow and behaves like a solid, but is fragile because the mixture can flow if the imposed stress is reduced or its direction is changed.[5] There is significant interest in understanding the mechanism behind the onset of shear thickening and the further transition into a jammed state.[6,7] Theories for the mechanism behind shear thickening involve the formation and growth of frictional force contacts between suspended particles.[8]

Insight into the balance of shear stress, volume fraction, and the underlying forces that influence cohesion has begun to be achieved through simulation techniques, including lubrication flow discrete element modeling (LF-DEM) which has recently enabled the simulation of flows of very dense particle suspensions by combining a short-range lubricating flow description for hydrodynamic interactions with a contact force model commonly employed in discrete element modeling of granular materials. This method has successfully reproduced key aspects of rheological behavior of dense suspensions such as a transition from CST to DST with increasing shear stress,[8,9] and inclusion of both attractive and Brownian forces has been demonstrated.[10,11] Including attractive forces (cohesion) has resulted in suspensions that exhibit both yielding and shear thinning at low stress and shear thickening and jamming at high stress.[12,13] Predicted flow-state diagrams for dense frictional suspensions that include attractive interactions contain an intermediate region of stress between the unyielded region and jammed states that is flowable, with shear thinning followed by shear thickening as stress increases.

Fundamental insight has begun to emerge regarding the role of contact friction force networks in rheological transitions, and on the relationships between clustering, network phenomena, and cohesive forces. A contact force network (CFN) is formed by considering the connections made between particle pairs that share a frictional force as the edges of a graph (network), with the particles being vertices. In this scenario, it is hypothesized that rupture of lubrication films between particles, as shear forces overwhelm a repulsive colloidal force, leads to shear thickening.[8,14,15] The central concept is that a CFN forms as particles are progressively driven into contact with one another, in this case by increasing imposed stress, and through the resulting connected structures the suspension resists flow more efficiently. Prior work[2,9,11,13,16,17] has shown that CFNs play a critical role in the rheological response of suspensions, both through their shear-induced rupture for yielding and their shear-induced formation in shear thickening. For example, the onset of shear thickening has been linked with the appearance and rapid growth of frictional contacts,[9] with this behavior being influenced by the presence of interparticle cohesive forces.[11] However, correlation of the various particle forces as a function of shear stress have not been extensively studied.

These insights have primarily been obtained through traditional analyses of the macroscopic response. However, network-based analyses and associated descriptors of network topology are beginning to contribute new insights into the mechanisms of rheological transitions.[2,18,19] Within a 2D suspension, Edens *et al.*[2] demonstrated that these network techniques could track the bulk rheological response of discontinuous shear thickening while also connecting that response to the global features of the force network. Topological descriptors that included the geodesic index and the void parameter were introduced to track the CFN response during shear thickening. These metrics reflected complementary aspects of the CFN, with the geodesic index tracking the connectedness of the contact network and the void parameter following the spatial areas devoid of particle contacts. Within the 2D system, the geodesic index revealed that the onset of DST was characterized by a rapid rise in the interconnectivity of the contact network, and was later complemented by topological data analysis,[20] which found that loops (network components of Betti number 1) were the most correlated with the rise in apparent viscosity. The void analysis provided insight into the homogeneous distribution of empty spaces, showing that the number and area of the voids were minimized uniformly during the increase in network connections. The implication is that within the 2D systems, the contact network grows homogeneously at large scales but with many local regions devoid of contacts.

Significant opportunities exist for applying network analyses to flowing suspensions. For example, characterizing the load-bearing networks as a function of shear stress in complex-rheology suspensions may provide fundamental insight into stress transmission and may guide the design of rheological modifiers within industrial applications, along with rigorous correlations to physicochemical particle forces. Here we expand upon our earlier work[2] by applying topological metrics introduced above to a 3D system.[13] The single volume fraction (ϕ) studied in this work can display both shear thinning and thickening behavior[9,21,22] and in the presence of attractive interactions (at sufficiently large ϕ) a suspension can even display yielding at low shear stress and thickening to a fully jammed state at high stress.[13,23] We compare and contrast the information content from various descriptors of geometric organization and network topology. Pair distribution functions, geodesic index analysis, and void analysis are employed along with a full breakdown of the forces networks involved, to elucidate the connection of particle microstructure and CFN evolution to both shear thinning and thickening processes. Analyzing the three-dimensional, non-Brownian cases from Singh *et al.*[13] allows us to further explore the particle dynamics that occur under different rheological conditions and the role played by the attractive interparticle forces.

2 Computational methods

LF-DEM is used to simulate simple-shear flows of dense suspensions.[8,9] We consider particle suspensions with different magnitudes of attractive interaction, which cause variation in both yield stress and the nature of shear thickening, *e.g.*, a large yield stress is found to obscure the shear thickening, as observed in silica particle suspensions with polymer-based depletion attractive forces[24] – a feature reproduced by the simulation method employed here.[11] Our goal is to elucidate the correlating relationships between geometric organization, viscosity, and the network of

forces (lubrication, contact and both attractive and repulsive conservative forces) between suspended particles. We first employ spatial correlation functions to quantify structural organization of the suspension in its transition from shear thinning to shear thickening. Next, the individual networks of lubrication, contact, and attractive forces are examined, both in the context of the distribution of forces in each network, and their interconnectivities and density.

2.1 Simulation protocol

Non-Brownian spherical particles interacting by lubrication hydrodynamics in a Newtonian fluid are simulated; conservative and frictional contact forces are included. 3D Lees–Edwards periodic boundary conditions[25] are employed with imposed stress so that the suspension flows at a time-dependent shear rate $\dot{\gamma}(t)$. We simulated about 500 total particles of equal volume fractions of bidisperse particles with radii a and $1.4a$ to prevent ordering. The unit cell for a simulation is shown with the two sizes shaded differently in Fig. 1 to provide an indication of the material packing density.

The particles experience short-ranged hydrodynamic (lubrication) forces $\mathbf{F}_H$, a conservative force $\mathbf{F}_{cons} = \mathbf{F}_A + \mathbf{F}_R$ (where A and R denote the attractive and repulsive parts of the interaction, respectively), and contact forces $\mathbf{F}_C$; in a compact notation, these quantities are actually the force and torque. We considered the motion to be inertialess (thus, zero Stokes and Reynolds numbers) so that the equation of motion is the force and torque balance on each particle,

$$0 = \mathbf{F}_H(\mathbf{R}, \mathbf{U}) + \mathbf{F}_C(\mathbf{R}) + \mathbf{F}_A(\mathbf{R}) + \mathbf{F}_R(\mathbf{R}), \quad (1)$$

where $\mathbf{R}$ and $\mathbf{U}$ are many-body position and velocity vectors; the velocity includes translation and rotation.

The conservative forces $\mathbf{F}_R$ and $\mathbf{F}_A$ are determined based on the positions of the particles, modeling the influence of physico-chemical parameters.

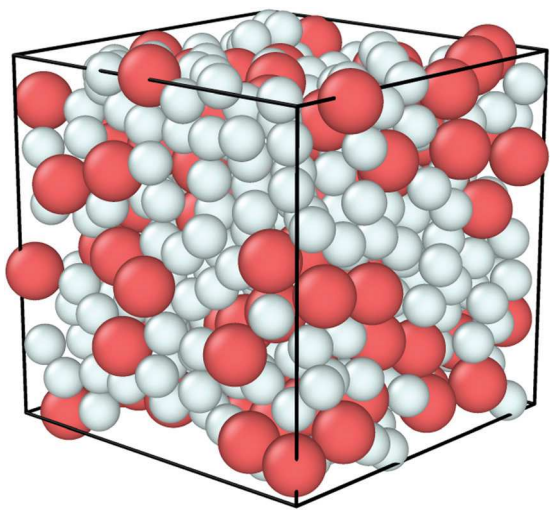

Fig. 1 Unit cell of the simulation, with 500 total particles of two radii a (lighter grey shading) and $1.4a$ (darker red shading). Each size particle makes up half of the particle volume fraction. This cell is replicated in all three directions and shearing is imposed by Lees–Edwards boundary conditions.

A detailed explanation of these forces is provided in previous work.[9,11,13] Briefly, the hydrodynamic forces are of the form

$$\mathbf{F}_H = -\mathbf{R}_{FU}\cdot(\mathbf{U} - \mathbf{U}^\infty) + \mathbf{R}_{FE} : \mathbf{E}^\infty \quad (2)$$

with $\mathbf{U}^\infty = \dot{\gamma}(t)y\hat{\mathbf{e}}_x$ being the flow due to imposed shear and $\mathbf{E}^\infty$ the associated rate-of-strain tensor described by $\mathbf{E}^\infty \equiv (\dot{\gamma}(t)/2)(\hat{\mathbf{e}}_x\hat{\mathbf{e}}_y + \hat{\mathbf{e}}_y\hat{\mathbf{e}}_x)$. The hydrodynamic resistance matrices $\mathbf{R}_{FU}$ and $\mathbf{R}_{FE}$ contain leading order terms corresponding to short-range lubrication forces.[26]

The occurrence of contacts between particles due, for example, to surface roughness is mimicked by regularizing the divergence of the resistance matrix at vanishing normalized interparticle surface separation between particles i and j, $h_{ij} = 2(d_{ij} - a_i - a_j)/(a_i + a_j)$ with d_{ij} the pair center separation: the "squeeze" mode resistance is proportional to $1/(h_{ij} + \delta)$, while the "shear" mode resistance is proportional to $\log(1/(h_{ij} + \delta))$.[9] Here, we have used $\delta = 10^{-3}$, such that the lubrication force is upper limited, and slight particle overlap (contact) is allowed.

The conservative forces used are shown in Fig. 2. A repulsive electrostatic double layer and attractive Van der Waals interaction between particles are modeled. The resulting force decays exponentially with interparticle surface separation as $|\mathbf{F}_R| = F_0\exp(-\hat{h}_{ij}/\lambda)$, where λ is the Debye length and $\hat{h}_{ij} = h_{ij}(a_i + a_j)/2$ is a dimensional interparticle separation. The attractive force between particles is described by $|\mathbf{F}_A(h_{ij})| = A\bar{a}/12(\hat{h}_{ij}^2 + H^2)$, where A denotes the Hamaker coefficient and $\bar{a}$ denotes the harmonic mean radius $\bar{a} = 2a_1a_2/(a_1 + a_2)$.[27] The parameter $H = 0.1\bar{a}$ is employed to eliminate the divergence of $\mathbf{F}_A$ at contact ($h_{ij} = 0$). The strength of attraction, F_A (=$|\mathbf{F}_A|$), is controlled by A, which determines the value of the attractive force at contact, $F_A(0)$

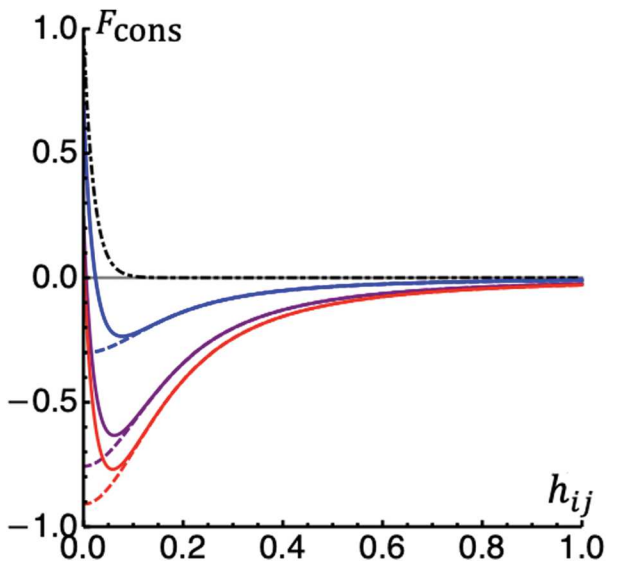

Fig. 2 Conservative forces $F_{cons} = F_A + F_R$, plotted as function of the scaled surface separation of a pair of particles, h_{ij}. The dash-dotted black curve represents the repulsive force; positive forces are repulsive. The dashed blue, purple, and red curves are the attractive force curves with maximum magnitudes at surface contact of $F_A = 0.3$, 0.75, and 0.9, respectively, with the solid curves of the same color representing the complete F_{cons} for the three values of attractive force.

(referred to as F_A in the rest of the article). To model the contact interaction between particles, we employ the approach of Cundall and Strack[28] using linear springs. However, there is no dashpot used here since the hydrodynamic resistance provides the source of energy dissipation. The tangential force between two particles satisfies $|\mathbf{F}_C^t| \leq \mu|\mathbf{F}_C^n|$ (*i.e.*, the Coulomb friction law) for compressive normal forces, where μ is the interparticle friction coefficient. Upon making contact, friction is activated and we fix the interparticle friction coefficient at $\mu = 1.0$. Sliding and non-sliding contact forces are not differentiated in this case. A finite softness is allowed at the contact. In this study, the spring stiffness is tuned for each (ϕ, σ), using a stiffer spring at large σ so that neither the normal nor tangential spring deformation exceeds $0.03a$, *i.e.*, they are maintained near the rigid limit;[9,29] it has been shown that the behavior can be reproduced using the maximum spring stiffness at all conditions, but with the cost of a much smaller time step at small stress,[15] apparently due to the need for sufficient deformation to allow enduring contacts; work without such deformation has shown that strong shear thickening is not captured.[30]

Using this simulation scheme, we determine particle positions (and thus conservative forces), normal and tangential contact forces, and non-contact lubrication forces. The development of the balance between contact and non-contact interactions with increasing strength of attraction is responsible for significant changes in the rheological response of the suspension. A detailed description of the viscosity response of frictional non-Brownian suspensions to increasing applied stress under various attractive forces can be found in Singh *et al.*[13] The apparent viscosity of the suspension is defined $\eta = \sigma/\dot{\gamma}(t)$, where σ is the imposed shear stress. The relative viscosity is $\eta_r = \eta/\eta_0$, where η_0 is the pure fluid viscosity. By increasing σ, these systems show a transition through two different shear response regimes. This response is shown in Fig. 3, modified from Singh *et al.*,[13] but here we focus on only the data that will be further analyzed below (*i.e.* 500 particle simulations with a volume fraction of $\phi = 0.56$). Beginning at low σ, all systems are in a soft solid state. With an increase in the applied shear stress beyond the yield stress, the suspension begins to flow and exhibits shear thinning, as the viscosity decreases with increasing σ. With further increase of the shear stress, the viscosity reaches a minimum and then increases in the shear thickening regime. The minimum viscosity occurs at a transition σ (in dimensionless form between 0.2 and 1.0, with scaling by F_0/a^2 that depends on F_A), and marks a shift from shear thinning to shear thickening. At larger σ, the viscosity continues to increase until a plateau is reached as the contact network growth, and thus the suspension viscosity, saturates. Increasing the F_A values results in a larger yield stress, and a shift to a larger value of the transition σ. The minimum viscosity values reached by shear thinning also increase with larger F_A, and for $F_A = 0.9$, it can be seen that the shear thickening is almost completely obscured, as the viscosity shear thins almost directly onto the high stress plateau. In short, increasing F_A increases the yield stress, leading to an increased rate of shear thinning as the connectivity is ruptured, and reduces the extent of shear thickening.

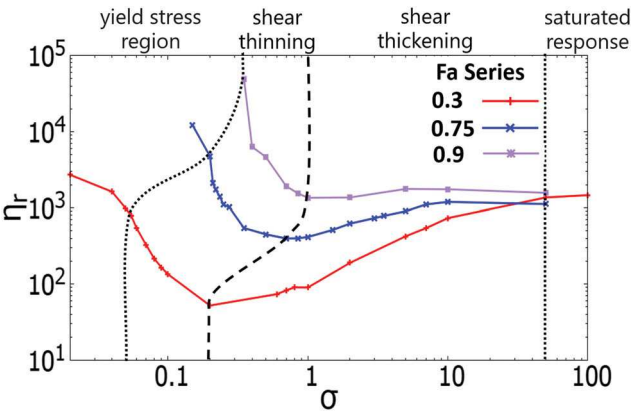

Fig. 3 Relative viscosity η_r plotted *versus* dimensionless applied stress σ (shown in log scale). The relative viscosity is $\eta_r = \eta/\eta_0$, where η_0 is the pure fluid viscosity. Each curve corresponds to a different global F_A value. The left and right dotted vertical lines separate flowing states from yield stress region and saturated response (*i.e.* shear-thickened) states as determined by Singh *et al.*[13] The middle dashed vertical line delineates the shear thinning to shear thickening transition.

2.2 Data analysis

2.2.1 Analysis of 3D particle configurations

Pair distribution functions. The pair distribution function (PDF) $G(d)$, was found by extensive sampling for the three pairs of particle sizes: small–small, large–small, and large–large based upon the interparticle distance d. Small and large particle radii are a and $1.4a$.

Void analysis in 3-dimensions. Given a collection of points in space, Voronoi analysis is a commonly used method that associates portions of space to their closest point in the collection. In the current work, the points are the particle centers, with the regions being Voronoi polyhedra. The Zeo++[31] open source software was utilized, as it is designed to perform geometry-based analysis of porous materials. The program utilizes three-dimensional Voronoi calculations to obtain the diameter of the largest free spheres, which provides the empty space void regions among a network of points. In this work, Zeo++ was employed in two ways. First, it was employed to study the changes in particle packing as a function of shear stress, to complement the information obtained from $G(d)$. In a more unique application of Zeo++, we subsequently analyzed the "voids" in the networks formed from contact forces. By manually defining the size of the input particles, Zeo++ can be utilized to find voids in 3D networks (essentially treating a network as a porous material). The "accessible volume", "pore size distribution", and "distance grids" functions were all utilized in this analysis. The accessible volume function outputs the number of voids, defined as either pockets (empty regions surrounded by particle network) or channels (empty regions where contiguous probe spheres overlap, extending across the bounding box). Together the pockets and channels define a pore, or overall void space. The LF-DEM output was converted to CSSR file format‡ and the outputs from Zeo++ were

‡ Information available at https://code.lbl.gov/.

averaged across all the snapshots. In all cases the probe sphere radius was set to the radius of the small particle to limit the probe to accessible volumes.

2.2.2 Network analyses. Network analysis is one method to characterize the topological organization of physical systems. Considering the different particle interactions, force networks can provide insight that is not apparent by observing solely particle location. We have used this analysis to identify correlations of particle force networks with the global structure, for example the creation of long chains *vs.* isolated pockets of particle–particle interactions, and with the bulk rheological response.

The adjacency matrix. A mathematical representation of a network is the $N \times N$ adjacency matrix $\mathbf{A}$. Two different representations of the force networks were examined. In the first, an unweighted network was analyzed; if the value of the specific type of force was above a cutoff threshold, then an edge value of 1 was given between a pair of particles and zero otherwise. For an unweighted network $\mathbf{A} = (\mathbf{A}_{ij})$ is defined as

$$\mathbf{A}_{ij} = \left\{ \begin{array}{c} 0 \\ 1, \text{ if } \alpha_{ij} \text{ is satisfied} \end{array} \right\} \quad (3)$$

where N is the number of participating nodes and α_{ij} is the criterion for establishing an edge between nodes i and j. The unweighted formalism is useful to identify a variety of network features, including the interconnectivity of the network and the voids in the network. For contact forces $\mathbf{F}_C$, an unweighted graph network is created by defining edges as the frictional contacts between particles. Frictional contact occurs when the center-to-center distance between particle pairs (d) is equal to the sum of the particles' radii $a_i + a_j$. In contrast to $\mathbf{F}_C$, the hydrodynamic (lubrication) forces, $\mathbf{F}_H$, and conservative force, $\mathbf{F}_{cons} = \mathbf{F}_A + \mathbf{F}_R$, are ranged interactions without hard cutoffs. To create an unweighted graph network for $\mathbf{F}_H$, a cutoff value was applied to the force values. Here an edge between particle pairs was established when the lubrication force value was above the 20th percentile of all lubrication force values for a given σ. In this work, the particle interaction forces are analyzed as separate networks and correlations are examined between those networks, as shown schematically in Fig. 4. Weighted force networks can be constructed when, in eqn (3), the weight of an edge between two particles is the actual value of the force (contact, lubrication, attractive, *etc.*) between the particles. Both weighted and unweighted networks were considered, and are constructed using the ChemNetworks software program.[32]

Measuring network interconnectedness. To consider the global topology of the network, we first consider pathways of interactions that span multiple nodes and can have a variety of forms, *e.g.* chains/strings or loops/cycles. The extent of interconnectivity within the network can be measured by analyzing the number of interaction pathways in which each node participates. It is mathematically expedient to define a shortest pathway that connects any pair of nodes, or a geodesic path. Here, the Floyd–Warshall (FW) algorithm[33,34] is used to convert $\mathbf{A}$ to the geodesic distance matrix containing the shortest contiguous interaction paths between individual nodes. The raw geodesic distance matrix contains all sub-paths that connect a pair of nodes (see Fig. S1, ESI†). These sub-paths are removed to create the so-called isolated geodesic matrix, the entries of which are used in the geodesic index, I_{gd}.[19,35] This metric of the normalized average number of pathways to which all nodes in the network contribute and converges with system size. The value of I_{gd} for a network with N nodes sampled at M frames of a simulation is given by

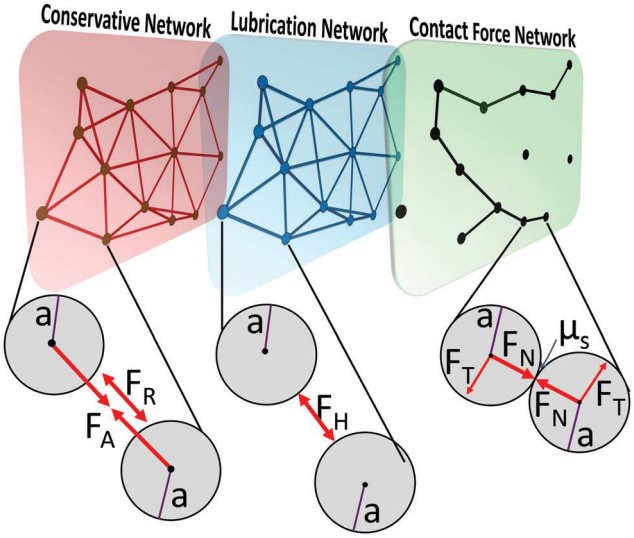

Fig. 4 A layered network, subdivided into the conservative, lubrication, and contact frictional force subnetworks. a is the small particle radius while F_N and F_T denote the force component normal and tangential to the contact respectively.

$$I_{gd} = 100 \times \left[\frac{\sum_{1}^{M} \rho_{gd}}{N \times M} \right]. \quad (4)$$

where

$$\rho_{gd} = \frac{gd_1 + gd_2 + \ldots + gd_N}{N}. \quad (5)$$

For $i = 1,\ldots,N$, gd_i is equal to the number of isolated geodesic paths in which node i participates. Note that ρ_{gd} can be larger than N, as node i can be a linking node in many geodesics that connect other pairs of vertices. The scaling factor of 100 is introduced for convenience.

Network sparsity. An analysis of regions void of frictional contacts was performed using the Zeo++[31] software. The same method that was utilized to find all particle voids was employed here, but applied on just the contact force network; particles that are not part of a contact pair (often called rattlers) were removed, *i.e.* only particles with at least one contact force edge were considered.

3 Results and discussion

3.1 Analysis of Cartesian space

3.1.1 Local geometric structure of the system. The pair distribution function (PDF) $G(d)$ indicates the likelihood of

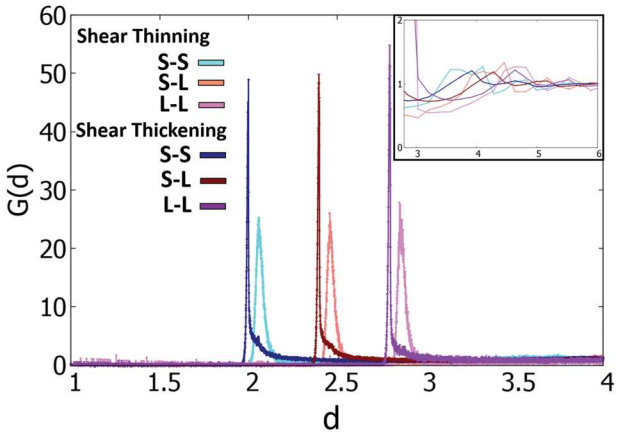

Fig. 5 A pair distribution function (PDF) plot for F_A = 0.3 where d is the particle pair distance (in units of particle radius a). The particle pair interactions for the bidisperse suspension have been separated by size, where small particles (*S*) have a normalized radius of 1 and large particles (*L*) have a radius of 1.4. Two shear stress values were plotted to highlight the difference between shear thinning (at σ = 0.055) and shear thickening (at σ = 5.0). Bin sizes were set to 0.001. The insert highlights secondary peaks for each pair interaction. Here the data has been smoothed using Bezier curves.

finding particles at a center-to-center distance d from the reference particle. The PDF for F_A = 0.3 between all particle pairs is shown in Fig. 5. The three data sets shown in Fig. 5 correspond to pairs of different particles sizes (1 : 1, 1 : 1.4, and 1.4 : 1.4). The PDF plots for all F_A datasets are included in the ESI† (see Fig. S2), along with a PDF plot for F_A = 0.3 where surface-to-surface distances are utilized (see Fig. S3, ESI†).

When adjusted for particle sizes, the three size pairings have similar $G(d)$, each with a main peak corresponding to the nearest-neighbor position. Integrating under the peaks from the PDFs yields the coordination numbers (CN) for the particle pairings (Fig. S4, ESI†). Overall, the distribution of CN for the interactions of different size particles indicate that the small particles are evenly dispersed between the larger ones. Besides a minor shift in $G(d)$ and CN values under higher F_A, there is little PDF variability across the three F_A values. In the shear thinning regime, all peak locations are at expected d values representative of the particles' respective sizes. Under shear thickening conditions, the peak d values and CN numbers indicate a slight tendency toward more tightly packed configurations within the particles forming the contact network. All F_A show a similar shift, as this is the result of the increased shear stress that forces the particles closer together.

3.1.2 Pore structure. The 3D spatial configurations of particles were explored by plotting the volume of empty domains (pores) as a function of σ (see Fig. S5, ESI†). A pore is defined as any space within the system that can contain a test sphere of radius a (the size of the smaller simulation particle) without the test sphere contacting any real particles. Tracking the total volume of pores conveys information about the spatial distribution of the system, highlighting any instances of large-scale inhomogeneity that occur as a function of shear stress. Regions of high density will produce many small pockets while low density regions will have larger void volumes. In this instance, pores show a relatively homogeneous distribution across all shear stress values for all F_A. However, the variability in the pore volumes decreases with increasing σ, showing that the particle reorganization accesses a narrower range of conditions in the shear thickening regime compared to the shear thinning regime.

Taken together, the $G(d)$ values, coordination numbers, and pore volumes all indicate that slight, but not striking, rearrangement of the geometric topology occurs as the systems transition across the shear thinning and shear thickening regimes. Therefore, the extreme changes observed in the viscosity are not a result of large-scale particle rearrangements and must instead be due to alteration of the balance of forces between particles, and reorganization of the networks they form. Thus, classical structural correlations give little insight, while we demonstrate below that the force network analyses provide guidance about these processes.

3.2 Layers of forces and their network interactions

Here, we consider the distributions of the particle interaction forces (conservative, lubrication, and frictional contact), paying particular attention to the differences observed when comparing the shear thinning and thickening regimes. All forces are scaled by the repulsive force $|F_R|$ at contact, which is actually a piece of the composite conservative force $F_A + F_R$. As the conservative forces depend only on position, *i.e.* on pair separation in this discussion, they will reflect and complement information gleaned from the pair distribution function. The lubrication forces are viscous and thus depend on particle relative motion.

3.2.1 Forces during shear thinning. In Fig. 6, the distributions of conservative, hydrodynamic lubrication, and contact forces are shown respectively in parts A–C, all for shear thinning conditions. All forces are determined pair-wise, so the distribution is expressed in the network theory term of an edge count, with a force conceived as an edge between two vertices that are the particles interacting through that force. In Fig. 6A, the conservative forces are characterized by a continuous distribution of attractive forces ($F_A + F_R < 0$), with distinct and sharp repulsive peaks evident for maximum (at surface contact) values of F_A = 0.75 and 0.9; the three peaks for each of these F_A values correspond to the three different particle size pair interactions (1 : 1, 1 : 1.4, and 1.4 : 1.4). The broad distribution is associated with sampling the full range of separations as particles approach and recede from one another, and is attractive as the attraction dominates except at close separations. The lack of added peaks for the shear-thinning conditions at contact value of F_A = 0.3 is a result of the point of zero force (PZF), *i.e.* where $F_A(r) + F_R(r) = 0$, being at a surface separation of about 0.04 radii, so the integrated effect of the weak repulsion and lubrication keeps the particles from making frequent contact, and thus the count is spread over many radial sampling points. For the higher attractions (maximum F_A = 0.75 and 0.9), the PZF is at surface separation of 0.01 or smaller, and the particles are pushed up to the maximum repulsive force for many samplings instead of distributed, leading to sharp peaks. Thus, even though the largest positive $F_A + F_R$ is largest for the case of a contact F_A = 0.3, this condition is not sampled densely

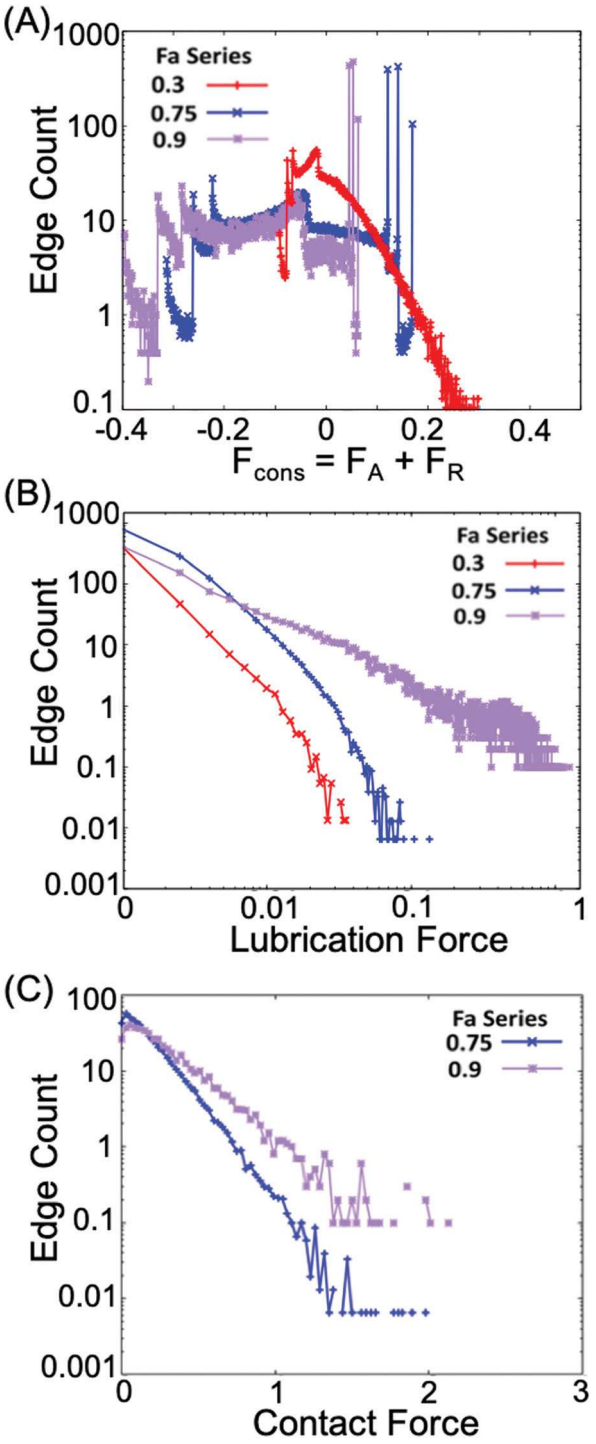

Fig. 6 Shear thinning condition force distribution. (A) Histogram of edge weights for total conservative force.(B) Histogram of edge weights in the lubrication force network. (C) log–Linear plot of the distribution of edge weights within the contact force network. The number of edges in the contact force network for F_A = 0.3 are virtually non-existent and are therefore not plotted. A lower cutoff value of 0.001 was utilized for edge weights. For all plots, σ values of 0.055, 0.21, and 0.3 were used for contact values of F_A = 0.3, 0.75, and 0.9, respectively.

at any one point, and essentially never at its maximum (surface contact) value for this low shear stress. Note that the absence of contact values of the extended-range conservative force is reflected in an absence of surface contact forces in Fig. 6C. The contact force network is relatively minor (with few edges) in the shear thinning regime. As shown in Fig. 6C, the contact forces begin to dominate over the conservative and lubrication forces for the larger F_A; interestingly, because force balance must be achieved on each particle, the implication is that the large contact forces are balanced by other contact forces and not by forces of a conservative or lubrication type. This has interesting rheological implications: while the yield stress increases with increasing strength of attraction, Singh *et al.*[13] reported that the contribution of viscosity due to contacts at the onset of flow increases with the strength of attraction. Our results confirm this, and show that this is due to the bringing of particles into proximity such that the flow occasionally induces a contact network. While the contact forces have significant strength, the values which are well above the scale of conservative and lubrication forces are relatively few, indicating that the contact force network is only occasionally dominant.

Fig. 6B shows the edge weight distribution within the lubrication force network, from which we may deduce certain dynamical features of the behavior. In the shear thinning regime, the lubrication edge weights increase at larger strength of attraction, as a result of particles being pulled close to contact, where the lubrication resistance (scaling as the inverse gap scale for normal motion) is largest. The lubrication forces are comparable to the conservative forces, with scaled values of $O(0.1)$, except for occasional large values at F_A = 0.9 where the noted PZF near contact results in contact network formation. When this network breaks, some particles have unbalanced contact forces and these must be balanced by rapid change of surface separation with neighbors, resulting in the large lubrication forces. Note that the edge count distributions of the elevated lubrication and contact forces at F_A = 0.9 are comparable, roughly falling in the range of 0.01–10.

3.2.2 Forces during shear thickening. Following the format of Fig. 6, the edge distribution within the conservative force network in the high stress shear thickening regime for the three F_A is shown in Fig. 7A. Again, the broad sampling of the attractive portion (negative force) is simply understood as a result of the bulk motion moving particles to and away from contact, thus sampling the longer-range attraction. We now see the sharp peaks in the conservative force distribution for all of the values of the attractive portion of the potential: these are the contact peaks where pair accumulation is indicated at contact in the $G(d)$ plots of Fig. 3. The peaks at maximum repulsion (positive $F_A + F_R$) for contact F_A = 0.3 are well-defined, but are lower in total edge count than the higher attraction forces. This is consistent with F_A = 0.3 having the least developed network organization. Both F_A = 0.75 and 0.9 show well-defined narrow peaks.

The edge weights of the lubrication forces for the shear thickening regime are smoothly distributed in magnitude, as seen in Fig. 7B. The lubrication forces, while generally more distributed to larger values than in the shear thinning regime, are dominated by the contact forces. Interestingly, the F_A = 0.9 shows the lowest lubrication force values while F_A = 0.3 has the

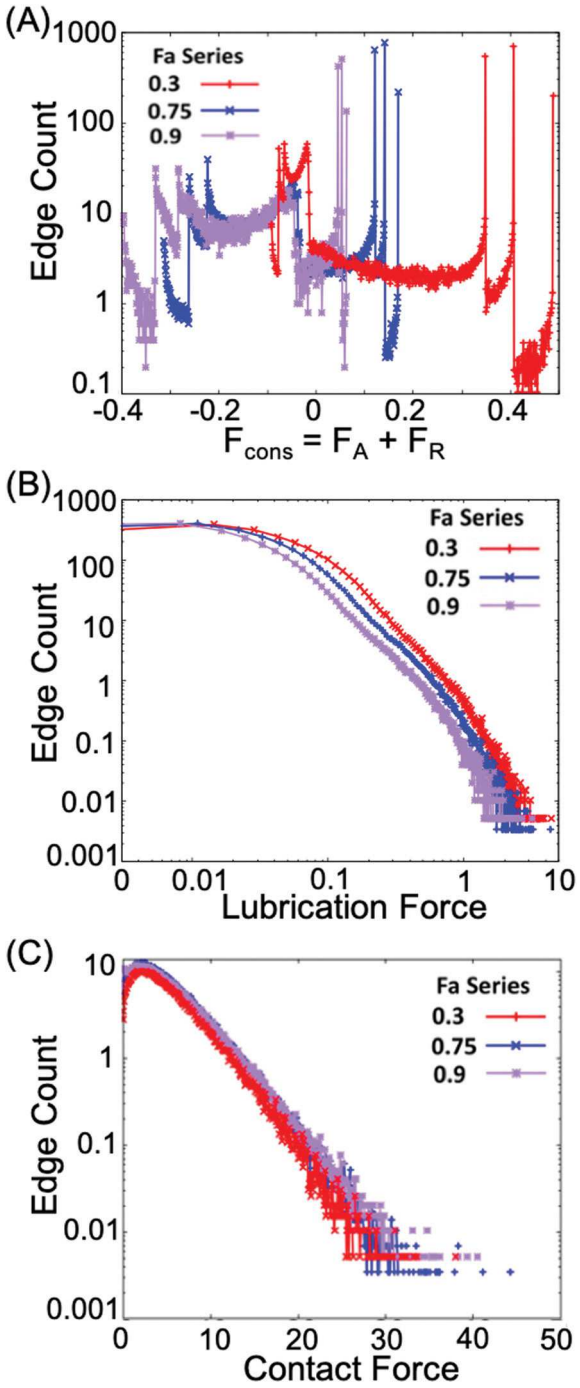

Fig. 7 Shear thickening condition force distribution. (A) Histogram of edge weights for total conservative force. (B) Histogram of edge weights in the lubrication force network. (C) log–Linear plot of the distribution of edge weights within the contact force network. A lower cutoff value of 0.001 was utilized for edge weights. For all plots, σ values of 5.0 were used.

highest value, suggesting that the stronger attraction is effective in generating correlated motion of sufficient solid-body character that larger lubrication forces are limited.

Contact forces are the dominant interactions during shear thickening, and significant edge counts extend to dimensionless force values of $O(10)$ where the shear thinning reached only $O(1)$. The contact forces for all three F_A are shown in Fig. 7C for $\sigma = 5$. The striking change in the contact force distribution between the thinning and thickening regimes highlights the transition from a lubricated to frictional rheology,[14,15] with the attractive forces playing a large role in the behavior at small stress. The form of the contact force distribution, with a large pair count for relatively small edge weights, a maximum corresponding to roughly the mean contact force, and an exponential decay at larger edge weights, is characteristic of the interparticle forces found in granular materials.[36] The relatively small differences in both lubrication and contact forces in the shear-thickening regime between different maximum F_A values point to the essential similarity of the material in this regime, with convergence to very similar bulk properties at $\sigma > 10$, where the attractive forces are small relative to the other forces.

3.2.3 Shear thinning *vs.* shear thickening regimes. Compared to shear thinning (Fig. 6), the attractive force network during shear thickening (Fig. 7) displays a slightly more organized structure, with $F_A = 0.3$ showing the most change. However, the overall attractive force edge distributions between particle pairs does not change significantly between the shear thinning and thickening regimes. With respect to the lubrication force network, as the suspension goes from shear thinning to shear thickening, the lubrication edge distribution display two major changes. First, the overall force magnitudes have greatly increased. Second, the relationship between the lubrication force and F_A reverses. Due to opposing factors, sorting out the exact mechanism behind these two changes in the lubrication response is difficult. While globally the overall particle distances do not greatly change between the shear thinning and shear thickening regimes, local distances in the shear thickening regimes can decrease. Lubrication requires relative motion between particles, and for a given relative motion (normal or tangential, with much stronger effects for normal motion), the force is stronger when the particle pair gap is smaller. It is possible that under shear thinning conditions, where contact forces are relatively insignificant, higher attraction forces pull more particles closer together, but not to contact. This increases pairwise lubrication forces and therefore the overall force scales with F_A. In the shear thickening regime, where contact forces are dominant over the other forces, larger σ values provide the force needed to drive more particles to contact.

Particles involved in frictional contributions have negligible relative motions along the line of centers of each pair. This leads to an appreciable reduction of lubrication forces at higher F_A, whereas the few particles that are not involved in such contact networks experience increased lubrication forces. The former contribution is dominant. Lower F_A values with higher lubrication forces thus aligns with the notion that structured local clustering due to dominant frictional contact forces is responsible for shear thickening.

Given the lack of a CFN in the shear thinning region, we analyze the changes to the contact forces by examining the growth of the network using two different metrics of network behavior, the geodesic index (a measure of interconnectivity and similar to betweenness centrality) and analysis of the void

regions in the network. The geodesic index, I_{gd}, is a global metric of the extent of interconnectivity in a network, as it measures how many nodes participate in isolated geodesic paths. We applied this measure to the frictional contact force networks. The geodesic index for all three F_A datasets is shown in Fig. 8A as a function of applied shear stress. For $F_A = 0.3$, the contact network is not significant until σ is large enough to be within the shear thickening regime. Once the transition σ value is reached, contact networks form rapidly as a function of σ, as indicated by the rising I_{gd}. At large σ, the geodesic index approaches its saturation value of particles participating in the network. For $F_A = 0.75$, I_{gd} has a value of ≈ 40 at $\sigma = 0.1$, indicating that the higher attraction force generates frictional contacts within the shear thinning regime, and continues to grow with uniform slope through the transition σ. For $F_A = 0.9$, I_{gd} begins at ≈ 60 at $\sigma = 0.1$ and shows a very rapid increase to the saturation value while still in the shear thinning regime, and in fact shows a slight overshoot, suggesting that the force network is a combination of shear-driven and attraction-driven contacts at the peak. I_{gd} then remains at its saturation value for all higher applied shear stress. This indicates that higher attractive forces allow for contact networks to form under shear thinning conditions. It is striking to note that I_{gd} correlates closely with the variation of the viscosity, explaining why shear thickening is essentially obscured at $F_A = 0.9$: the saturated network is essentially fully developed in the thinning regime, whereas at lower F_A, saturation of the occurs at stresses above the transition value and so the viscosity exhibits significant shear thickening.

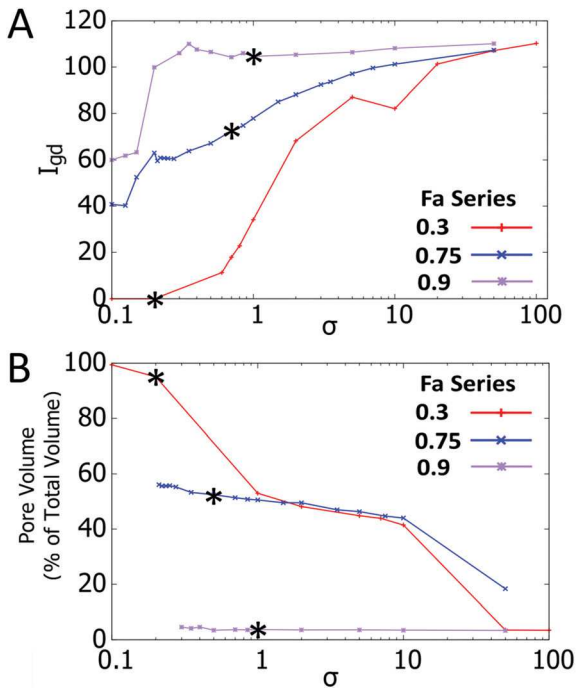

Fig. 8 (A) The geodesic index for contact networks (shown in log scale). (B) The total pore volume (*i.e.* empty space) created by the contact networks plotted as a percentage of maximum possible pore volume. For all plots, each curve corresponds to a different F_A value. The asterisks represent the transition point between shear thinning and shear thickening.

Complementary to the connectivity measure of the geodesic index is an understanding of the regions that remain unoccupied by the contact networks as stress increases. We begin by describing the pore data and continue by relating the results to the geodesic index. Measuring volumes of the empty domains, or pores, conveys information on the patterns associated with the forming networks. Here the edges of the contact network form the boundaries that segregate the void domains; therefore, a region of high connection density will produce many small voids. Under increasing σ, a uniformly growing network will show a continuous, rapid decrease in pore volume as network connections spread across the empty domains. Conversely a network grown inhomogeneously from several "seed" locations will initially display a slow decrease in pore volume, switching to a rapid decrease when the various networked domains connect with each another.

The pore volume (as a percentage of the total possible empty volume) for all three F_A is shown in Fig. 8B as a function of applied shear stress. As expected from the above geodesic plot, the $F_A = 0.3$ dataset shows the most change in pore space while $F_A = 0.9$ only has very small pores resulting from a saturated network. However, there is new information in the shape of each curve. $F_A = 0.3$ initially shows a very rapid decrease until $\sigma = 1$. This is indicative of a uniformly spreading network that rapidly forms across the empty domains. Within the shear thickening regime, between $\sigma = 1.0$ and $\sigma = 10$ the decrease in pore volume slows. The slow growth appears to result from contacts spreading from established zones, consistent with the formation of a fully ramified CFN from more tenuous contact force chains. At large σ, the pore volume rapidly decreases again as the local networks meet each other and form a saturated global network. In contrast, $F_A = 0.75$ does not exhibit a rapid decrease of pore area, but instead shows a steady decrease in pore volume until near global saturation. Interestingly, between $\sigma = 1.0$ and $\sigma = 10$, both $F_A = 0.3$ and $F_A = 0.75$ have similar pore volumes and show similar network growth. However, the lack of an initial global homogeneous growth pattern for $F_A = 0.75$ may mean the contact networks present have many small zones of high connectivity, which could explain why I_{gd} for that network remains greater than for $F_A = 0.3$.

4 Conclusions

In-depth knowledge of the rheological response of dense suspensions is critical to handle, predict, and tailor flows of the suspensions in various natural (*e.g.*, sediments, mud) and industrial (*e.g.*, petroleum, ceramic, cement, and nuclear waste treatment) settings. Utilizing detailed information on positions and forces associated with the particles from the LF-DEM simulations, we have investigated correlations between geometric organization of particles, underlying forces, and rheological properties based on different spatial analyses and topological metrics exhibiting global/local particle organization and connectivity, combined with network structure/topology and strength of particle forces. Specifically, we implemented pair distribution functions, and geodesic index/void analyses, combined with detailed force analysis, to explain

the particle microstructure and contact force network behavior during both shear thinning and thickening processes.

These analyses demonstrate that changes to suspension viscosity do not simply result from local/global-scale particle rearrangements but are rather associated with the detailed balance of forces between particles and resultant force networks, coupled with the application of shear stress. For the force network analyses, global metrics (*e.g.*, geodesic index and pore volume) present reasonable signatures of ensemble characteristics of rheology, here shown as the relative viscosity, of suspensions, connecting to the balances between particle forces. This can provide a connection between parameters used in empirical viscosity models of dense suspensions (*e.g.*, Krieger–Dougherty equation) and structural information for attractive dense suspensions. The network analyses indicate that significant rearrangements of the balance of forces occur as a suspension transitions from shear thinning to shear thickening with application of shear stress. The attractive, lubrication, and contact force networks evolve in an interactive fashion as the regime changes. Although the attractive force is dominant under shear thinning, with increased σ, lubrication force networks grow that oppose attraction and both become outweighed by the contact force network as shear thickening occurs. As understood from prior study, contact forces dominate during shear thickening – increasing by an order of magnitude across the shear thinning to shear thickening transition. Interestingly, the growth of the contact force network, and more specifically the network topology, is rather sensitive to the magnitude of the attractive interaction between particles within the simulation. For example, at smaller attractive force, different rates of the network topology growth rate can be observed once the shear thinning – shear thickening transition is reached. In contrast, under sufficiently large attractive force, these different growth rates are absent from the network topology and contact networks saturate during the shear thinning regime. In addition, the manner in which the contact force network grows in these 3D suspensions is more nuanced than previously observed in 2D suspensions analysed using a similar methodology. This highlights a need for more quantitative correlations between the interaction network and rheological responses.

Conflicts of interest

There are no conflicts to declare.

Acknowledgements

This research was supported by the Interfacial Dynamics in Radioactive Environments and Materials (IDREAM), an Energy Frontier Research Center funded by the U.S. Department of Energy, Office of Science, Basic Energy Sciences. PNNL is a multiprogram national laboratory operated for DOE by Battelle Memorial Institute under Contract No. DE-AC05-76RL0-1830. JFM's contributions were supported by the National Science Foundation Award 1916879, with CCNY computations supported by NSF grant numbers CNS-0958379, CNS-0855217, and ACI-1126113 at the CUNY High Performance Computing Center at the College of Staten Island.

Notes and references

1 J. Mewis and N. J. Wagner, *Colloidal Suspension Rheology*, Cambridge University Press, 2011.
2 L. E. Edens, S. Pednekar, J. F. Morris, G. K. Schenter, A. E. Clark and J. Chun, *Phys. Rev. E*, 2019, **99**, 012607.
3 E. Del Gado and J. F. Morris, *J. Rheol.*, 2020, **64**, 223–225.
4 G. Chatté, J. Comtet, A. Nigués, L. Bocquet, A. Siria, G. Ducouret, F. Lequeux, N. Lenoir, G. Ovarlez and A. Colin, *Soft Matter*, 2018, **14**, 879–893.
5 R. Seto, A. Singh, B. Chakraborty, M. M. Denn and J. F. Morris, *Granular Matter*, 2019, **21**, 82.
6 E. Brown and H. M. Jaeger, *Rep. Prog. Phys.*, 2014, **77**, 046602.
7 S. Gürgen, M. C. Kushan and W. Li, *Prog. Polym. Sci.*, 2017, **75**, 48–72.
8 R. Seto, R. Mari, J. F. Morris and M. M. Denn, *Phys. Rev. Lett.*, 2013, **111**, 218301.
9 R. Mari, R. Seto, J. F. Morris and M. M. Denn, *J. Rheol.*, 2014, **58**, 1693–1724.
10 R. Mari, R. Seto, J. F. Morris and M. M. Denn, *Proc. Natl. Acad. Sci. U. S. A.*, 2015, **112**, 15326–15330.
11 S. Pednekar, J. Chun and J. F. Morris, *Soft Matter*, 2017, **13**, 1773–1779.
12 A. Singh, R. Mari, M. M. Denn and J. F. Morris, *J. Rheol.*, 2018, **62**, 457–468.
13 A. Singh, S. Pednekar, J. Chun, M. M. Denn and J. F. Morris, *Phys. Rev. Lett.*, 2019, **122**, 098004.
14 M. Wyart and M. E. Cates, *Phys. Rev. Lett.*, 2014, **112**, 098302.
15 J. F. Morris, *Phys. Rev. Fluids*, 2018, **3**, 110508.
16 J. R. Melrose and R. C. Ball, *J. Rheol.*, 2004, **48**, 961–978.
17 R. Mari and R. Seto, *Soft Matter*, 2019, **15**, 6650–6659.
18 L. Papadopoulos, M. A. Porter, K. E. Daniels and D. S. Bassett, *J. Complex Netw.*, 2018, **6**, 485–565.
19 A. E. Clark, *Annual Reports in Computational Chemistry*, Elsevier, 2015, vol. 11, pp. 313–359.
20 M. Gameiro, A. Singh, L. Kondic, K. Mischaikow and J. F. Morris, *Phys. Rev. Fluids*, 2020, **5**, 034307.
21 D. R. Foss and J. F. Brady, *J. Fluid Mech.*, 2000, **407**, 167–200.
22 A. Boromand, S. Jamali, B. Grove and J. M. Maia, *J. Rheol.*, 2018, **62**, 905–918.
23 I. R. Peters, S. Majumdar and H. M. Jaeger, *Nature*, 2016, **532**, 214–217.
24 V. Gopalakrishnan and C. F. Zukoski, *J. Rheol.*, 2004, **48**, 1321–1344.
25 A. W. Lees and S. F. Edwards, *J. Phys. C: Solid State Phys.*, 1972, **5**, 1921.
26 R. C. Ball and J. R. Melrose, *Phys. A*, 1997, **247**, 444–472.
27 W. B. Russel, D. A. Saville and W. R. Schowalter, *Colloidal Dispersions*, Cambridge University Press, 1992.
28 P. A. Cundall and O. D. L. Strack, *Geotechnique*, 1979, **29**, 47–65.
29 A. Singh, V. Magnanimo, K. Saitoh and S. Luding, *New J. Phys.*, 2015, **17**, 043028.

30 A. K. Townsend and H. J. Wilson, *Phys. Fluids*, 2017, **29**, 121607.
31 T. Willems, C. Rycroft, M. Kazi, J. Meza and M. Haranczyk, *Microporous Mesoporous Mater.*, 2012, **149**, 134–141.
32 A. Ozkanlar and A. E. Clark, *J. Comput. Chem.*, 2014, **35**, 495–505.
33 R. W. Floyd, *Commun. ACM*, 1962, **5**, 345.
34 S. Warshall, *J. Assoc. Comput. Mach.*, 1962, **9**, 11–12.
35 C. H. Wang, P. Bai, I. Siepmann and A. E. Clark, *J. Phys. Chem. C*, 2014, **118**, 19723–19832.
36 D. M. Mueth, H. M. Jaeger and S. R. Nagel, *Phys. Rev. E: Stat. Phys., Plasmas, Fluids, Relat. Interdiscip. Top.*, 1998, **57**, 3164.